Four-dimensional chromosome reconstruction elucidates the spatiotemporal reorganization of the mammalian X chromosome

Anna Lappala[a,b,c], Chen-Yu Wang[b,c], Andrea Kriz[b,c], Hunter Michalk[a], Kevin Tan[b,c], Jeannie T. Lee[b,c,1], and Karissa Y. Sanbonmatsu[a,d,1]

[a]Theoretical Biology and Biophysics, Los Alamos National Laboratory, Los Alamos, NM 87545; [b]Department of Molecular Biology, Massachusetts General Hospital, Boston, MA 02114; [c]Department of Genetics, The Blavatnik Institute, Harvard Medical School, Boston, MA 02114; and [d]New Mexico Consortium, Los Alamos, NM 87545

Contributed by Jeannie T. Lee, August 24, 2021 (sent for review April 14, 2021; reviewed by Vadim Backman and Musa Mhlanga)

Chromosomes are segmented into domains and compartments, but how these structures are spatially related in three dimensions (3D) is unclear. Here, we developed tools that directly extract 3D information from Hi-C experiments and integrate the data across time. With our "4DHiC" method, we use X chromosome inactivation (XCI) as a model to examine the time evolution of 3D chromosome architecture during large-scale changes in gene expression. Our modeling resulted in several insights. Both A/B and S1/S2 compartments divide the X chromosome into hemisphere-like structures suggestive of a spatial phase-separation. During the XCI, the X chromosome transits through A/B, S1/S2, and megadomain structures by undergoing only partial mixing to assume new structures. Interestingly, when an active X chromosome (Xa) is reorganized into an inactive X chromosome (Xi), original underlying compartment structures are not fully eliminated within the Xi superstructure. Our study affirms slow mixing dynamics in the inner chromosome core and faster dynamics near the surface where escapees reside. Once established, the Xa and Xi resemble glassy polymers where mixing no longer occurs. Finally, Xist RNA molecules initially reside within the A compartment but transition to the interface between the A and B hemispheres and then spread between hemispheres via both surface and core to establish the Xi.

X chromosome inactivation | Xist RNA | chromosome structure | SMCHD1 | 3D modeling

The dynamics and structural reorganization of chromosomes contribute to important physiological transitions in the cell. Three-dimensional (3D) chromosome structure information is critical for understanding their dynamics and the extent to which gene expression and epigenetic mechanisms are regulated by the 3D architecture of chromatin (1, 2). Breakthrough technological advances, such as Hi-C, have enabled large-scale sequencing of genome-wide two-dimensional (2D) contacts (3) and validated earlier observations that mammalian chromosomes are organized into loop domains, anchored by CCCTC-binding factor (CTCF) proteins, and into larger compartments, which roughly correlate with gene-expression states (4–9). While it is well-established that long-range loops between regulatory elements, such as enhancers and promoters, play a role in developmentally timed gene expression (10–12), studies have also shown that abolition of topological domains and major shifts in compartmentalization have little immediate impact on gene expression (13–19). These studies have therefore left open the question of whether and how chromosome structure regulates gene expression. Novel protocols have been developed to label genes for live-cell imaging to study chromatin dynamics (20), but new methodologies are still required to push the present boundaries of knowledge. While there are models that demonstrate important specific features of chromosome architecture (21–23), critically missing are methodologies that directly convert 2D biological information (such as from Hi-C contact maps) into 3D models of the chromosome. Such methodologies could yield valuable models from large-scale sequencing experiments of the pairwise contacts that make up 2D contact maps.

Hi-C experiments typically yield a genome-wide composite of long-distance interactions between two genetic loci. For every set of 2D experimental data, however, there are many possible 3D folds that would be consistent with the aggregate of pairwise interactions. Resolving the 3D structure could therefore be challenging, as connectivity information alone does not provide all the information needed to generate a 3D structure because only relative 2D positions (deduced from cross-linked contacts that are preserved through DNA ligation) are defined and no actual 3D contacts are directly visualized. Over the past decade, various methods for 3D modeling had been developed (21, 24, 25), and these can be roughly classified into two groups: "mechanistic" and "inverse" models (for a full review, see ref. 26). Mechanistic models (27, 28) provide detailed structures of gene loci. Inverse models use data to infer chromatin structures, generating in silico configurations of gene loci or whole chromosomes consistent with Hi-C data. A prominent example of a constraint-based inverse

Significance

Breakthrough technological advances such as Hi-C have enabled large-scale sequencing of pairwise genomic contacts. However, translating the 2D contacts to 3D spatial models remains challenging. Here we develop the "4DHiC" modeling method to infer 3D information from 2D datasets across time and construct a 3D model of the inactive X-chromosome (Xi). Our model not only demonstrates a spatial phase-separation between A/B and S1/S2 compartments to form "hemispheres," but also reveals persistent smaller-scale structures hidden under the Xi superstructure. We also simulate Xist RNA spreading dynamics and deduce that the RNA spreads between hemispheres via both surface and core to establish the Xi. Our 4DHiC will serve a growing demand for data-driven methodologies that extract spatial information from biochemical interaction data.

Author contributions: A.L., J.T.L., and K.Y.S. designed research; A.L. and K.Y.S. performed research; A.L., C.-Y.W., H.M., K.T., and K.Y.S. contributed new reagents/analytic tools; A.L., C.-Y.W., A.K., K.T., J.T.L., and K.Y.S. analyzed data; and A.L., J.T.L., and K.Y.S. wrote the paper.

Reviewers: V.B., Northwestern University; and M.M., Radboud Institute for Molecular Life Sciences.

Competing interest statement: J.T.L. is a cofounder of Translate Bio and Fulcrum, and is an advisor to Skyhawk Therapeutics.

[1]To whom correspondence may be addressed. Email: lee@molbio.mgh.harvard.edu or kys@lanl.gov.

This article contains supporting information online at https://www.pnas.org/lookup/suppl/doi:10.1073/pnas.2107092118/-/DCSupplemental.

Published October 13, 2021.

model includes TADbit, which has been used to reconstruct gene loci in mammalian cells (24). Similar methods have been applied to reconstruct whole yeast nuclei (29). Thus, there are a variety of computational approaches that could potentially be applied to synergize with the biochemically based Hi-C datasets. Previous efforts have employed polymer simulations from first principles with great success, incorporating well-defined one-dimensional (1D) information, such as CTCF motifs, reconstructing 2D connectivity profiles from first principles (21, 23, 30). This approach has been successful in identifying critical elements of chromatin organization, such as loops, leading to the proposed mechanism of chromatin folding by loop extrusion (21). These previous models performed by other groups provide a possibility to generate a contact map assuming that the 1D information is sufficient for such predictions. However, there could be unknown factors and motifs that might change the model as new experimental techniques emerge.

To minimize assumptions and biases, here we ask the questions: Given Hi-C data, can a model be generated such that all 2D biological information is mapped directly onto the 3D structure without assumptions and prior knowledge of the epigenetic modification state of the chromosome, and can a modeling pipeline be developed that would be transferable to any Hi-C dataset? Indeed, here, we develop "4DHiC" (pronounced "4-D-Hi-C") that enables visualizing chromosomes in 3D over time. We test the approach on a classic epigenetically regulated chromosome: the inactive X (Xi) of the female mammal. In female mammals, one X chromosome is transcriptionally inactivated to balance gene expression between females and males. X-chromosome inactivation (XCI) involves a progressive transformation of an active X chromosome (Xa) to an Xi, precipitated by Xist RNA molecules spreading over the chromosome (31–34). Many 1D (e.g., epigenetic sequencing) and 2D (e.g., Hi-C) studies of XCI have been performed and together they point to three evolving principles of chromosome organization (Fig. 1*A*): 1) A/B compartments, delineating active and inactive regions on the Xa (7); 2) S1/S2 compartments, appearing during the transition from Xa to Xi (35); and 3) two megadomains, a structural endpoint for the Xi (7, 14, 36–39). These studies have complemented a wealth of microscopy studies regarding the large-scale organization of the Xi in the nucleus (40–46). Yet, many open questions remain. What is the relationship between A/B and S1/S2 compartments? Are S1/S2 structures transitory or do they persist during XCI? How do megadomains form? Finally, how does Xist RNA spread over the evolving 3D Xi geometry? To address these questions, we apply 4DHiC, reveal the 3D Xi structure across time, and observe features not previously detected by classic Hi-C analysis.

Results

Three-Dimensional Reconstructions from Hi-C with 4DHiC. Our 4DHiC approach applies the inverse method with the distinguishing feature that a minimal number of underlying assumptions are imposed regarding chromosome structure. For example, no assumptions are made regarding how compartments interact with each other or whether specific genes, chromosomal regions, or proteins (such as CTCF) are critical for structure formation. Additionally, 4DHiC does not stipulate that the distances between Hi-C interacting beads need be inversely proportional to their interaction frequency, as such stipulation could undesirably distort chromosome structure by forcing beads with weak interaction strengths to be farther apart, when in fact they could be merely beyond cross-linking distance. In 4DHiC, by using harmonic constraints to simulate cross-linking distances, we achieve direct, experimentally validated correspondence between the 3D model and the experimentally determined Hi-C contact map, allowing us to visualize complex features observed on a 2D Hi-C map in 3D without prior assumptions about any features in the Hi-C maps. Thus, empirically determined pairwise interactions from Hi-C experiments are directly converted to a 3D rendering, with a time dimension added subsequently on the basis of changes observed during a Hi-C time course. Our approach bypasses the need to call topological domains, loops, compartments, and other classic structures evident in Hi-C contact maps.

Our approach instead uses a coarse-grained polymer model and is scalable: the number of beads can be increased or decreased, allowing tuning of the resolution of the polymer to the resolution of any Hi-C dataset (Fig. 1*B*). The approach does not rely on the multidimensional (MD) scaling approximation, which infers 3D distances based on measured contact frequency (47). We adapted the polymer bead-spring model from Grest and Kremer (48), a widely used polymer model that describes a polymer as beads connected by springs (48, 49). Our Hi-C datasets for X inactivation have a resolution of 200 kb. Thus, we modeled the 166-Mb X chromosome as a polymer with 833 beads, with one bead for each Hi-C bin viewed at 200-kb resolution. We began with a random polymer chain conformation and generated a 3D model by collapsing the polymer using a self-avoiding random walk and imposing constraints based on strongly attracting monomers (i.e., guided by the empirically measured pairwise *cis*-interactions captured by Hi-C experiments). Simulations are continued until convergence is achieved between simulated 2D contact maps and experimentally determined 2D Hi-C maps (correlation coefficient R ~0.97) (Fig. 1).

Validation of the Hi-C Method. To validate our 4DHiC pipeline, we first reconstructed the Xa and colored two halves of the chromosome separated by the microsatellite repeat, *Dxz4* (Movie S1) (7, 14, 18, 36, 39, 50): a centromeric (CEN) half in white corresponding to the proximal megadomain on the Xi (0 to 72 Mb) and a telomeric (TEL) half corresponding to the distal megadomain on the Xi (73 to 166 Mb) in purple (Fig. 1). Without constraints, the model polymer chain folded into a 3D structure without apparent organization (*SI Appendix*, Fig. S1), as expected, with the two halves (white, purple) of the Xa fully mixed in 3D (Fig. 1 *C*, *Left*). On the other hand, constraining the model using empirically measured 2D Hi-C contacts generated an orderly 3D chromosome model, with the proximal and distal halves of the Xa separated into two poles (Fig. 1 *D*, *Left*). The simulation-derived 2D contact map correlates strongly with the Hi-C–derived map ($R_{cp} = 0.97$, $R_{Pearson} = 0.85$) (Fig. 1 *D*, *Right*). In particular, although the long-range interactions required for Xi megadomains are not present in the Xa, the two chromosomal halves still undertook compact globular morphologies that were spatially separated from each other in 3D space, consistent with previous studies (46). We also studied the effect of deletion of Dxz4 on the structure of the X chromosome based on Darrow et al. (14), and our 3D models were consistent with previous empirical findings (*SI Appendix*, Fig. S2) and other models based on genome architecture mapping (GAM).

We then asked whether the 4DHiC pipeline could model the multimegabase, alternating A and B compartments in a principal component analysis (PCA) of Hi-C data. In the first principal component (PC1) of the Xa, active chromatin roughly correlates with the A compartment (positive value eigenvectors), while silent chromatin roughly correlates with the B compartment (negative values) (Fig. 1 *E*, *Lower Inset*). For each region of the chromosome (i.e., bin of the Hi-C map), a connectivity profile is determined (row of contact matrix); a covariance matrix is calculated from covariation of profiles; in the initial basis set, each dimension corresponds to a chromosome region (bin); the covariance matrix is then diagonalized by finding a new basis set (consisting of linear combinations of regions) that maximizes the collective variation of profiles with across the chromosome. The first eigenvector (PC1) is composed of a linear combination of a special subset of bins whose connectivity profiles are the most highly coupled. This subset includes, but is not limited to, boundaries between spatially localized domains. The collective coordinate (PC1) often couples many regions that are distant from each in sequence space but

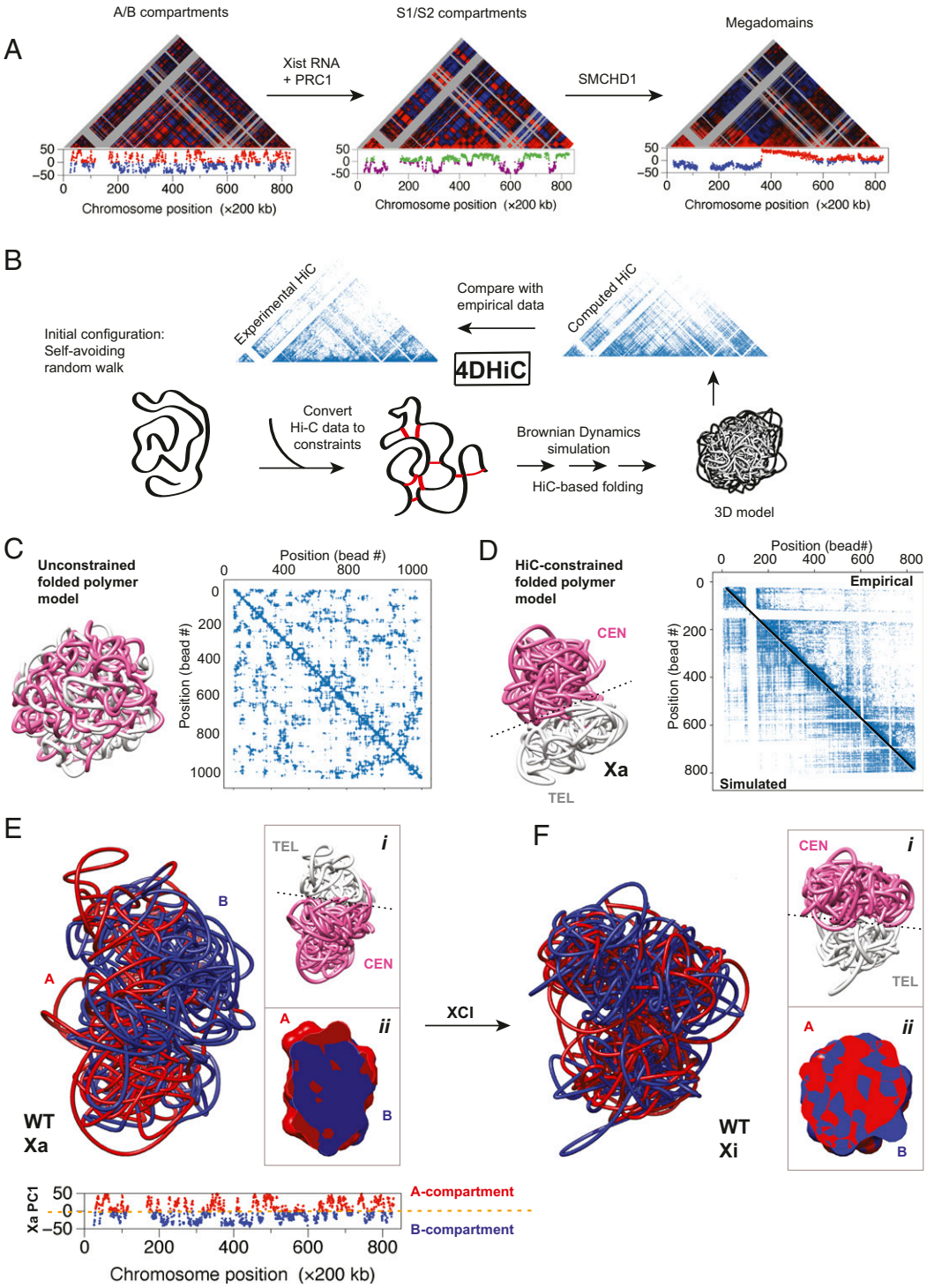

Fig. 1. Three-dimensional reconstructions of Xa and Xi using our 4DHiC pipeline. (*A*) Schematic of megadomain formation during XCI showing Pearson correlation maps and PC1 at each stage. Adapted from ref. 35, with permission from Elsevier. (*B*) Schematic of 4DHiC pipeline: virtual cross-links are created from experimentally determined Hi-C maps and applied to a beads-on-string polymer model of chromosome with self-avoiding random 3D structure; MD simulations with constraints produce a folded chromosome structure; simulated Hi-C map is computed from folded structure; simulated map is compared with experimentally determined map; MD simulations proceed until convergence between simulation and experiment is achieved. (*C*) Results of the unconstrained folded polymer model (folded equilibrium globule) shows mixing of CEN and TEL regions. Pink, the region corresponding to megadomain 1 (positions 0 to 73 Mb); white, the region corresponding to megadomain 2 (positions 73 to 166 Mb). Contact map for a folded equilibrium globule shows extensive mixing within the chain. The matrix is divided into two triangles, with each showing the same pairwise comparison and data taken from an unconstrained "randomized" model. (*D*) Three-dimensional model of the WT Xa. Comparison between experimental (*Upper Right* triangle) vs. simulated (*Lower Left* triangle) Hi-C contact maps for the WT Xa shows agreement. (*E*) A/B compartments defined by PC1 of Xa projected onto 3D reconstruction of Xa shows spatial separation between A and B compartments. Red: positive values in PC1; blue: negative values. (*i*) Regions corresponding to megadomains (colors same as *D*). (*ii*) Cross-section. (*Lower inset*) PC1 vs. 1D sequence position shows that A and B compartments are mixed in 1D sequence space. (*F*) Three-dimensional reconstruction of Xi showing mixing of *A* and *B* compartments in 3D physical space (colors same as *E*) (*i*): Regions corresponding to megadomains (colors same as *D*). (*ii*) Cross-section.

span the entire chromosome. Because PC1 data are 1D, how compartments are spatially related in 3D is not immediately clear. The ability to visualize this spatial connectivity is beneficial for structure–function analysis.

The first challenge was to map the A/B compartments derived from PC1 of Xa (Fig. 1 *E*, *Lower*) to a 3D reconstructed model of the Xa. Here, positive PC1 values represent A compartments, which are strongly coupled in terms of how their connectivity profiles vary with respect to one another; negative values represent the more-weakly coupled B compartments. Using allele-specific Hi-C reads mapping to the Xa, we colored A and B regions red and blue, respectively, and mapped their positions onto the CEN (pink) and TEL (white) halves of our deduced Xa model (Fig. 1*E*). The A/B compartments of the Xa appeared segregated in 3D space into red and blue regions, with little mixing between regions. Thus, the A and B compartments do not merely have opposite gene-expression states and epigenetic marks but are also spatially segregated on opposite faces of the Xa in an orientation that is roughly orthogonal to the TEL/CEN axis (compare the red/blue model with the white/pink model in Fig. 1 *E*, *i*). Further information could be gathered by examining tomographic sections of the Xa model. Intriguingly, there is a clear spatial phase separation of A and B extending into the core of the Xa (Fig. 1 *E*, *ii*), enabling the visualization of Xa compartments in 3D. In this context, we argue for a spatial phase separation on the basis of physical clustering of the compartments and chromatin with distinct epigenetic features.

Xi Transition from A/B to S1/S2 Organization in 3D. An unresolved question is what happens to the A/B compartments during the time-dependent process of XCI. Previous work showed that, as ∼63 A/B compartment regions are reorganized on the X chromosome, ∼25 S1/S2 regions appear, directed to form by Xist RNA together with Polycomb repressive complex 1 (PRC1) (51). The spatial relationship between A/B and S1/S2 compartments is unclear. Are the A/B structures destroyed in order to form S1/S2 compartments? Does the chromatin relocate in order to reorganize into S1/S2 structures? These two scenarios would be energetically unfavorable because of the need to destroy preexisting structures and to construct new structures. An alternative, more energetically favorable mechanism would entail building upon, rather than destroying, preexisting structures.

To address these questions, we modeled the 3D structure of the Xi using allele-specific data from Hi-C experiments taken from mouse neural progenitor cells. The Xi also partitioned in an orderly way into a CEN and TEL halves (Fig. 1 *F*, *i*). However, when A/B compartments from Xa were mapped onto the 3D Xi, there was a clear mixing of red and blue A/B compartments (Fig. 1*F*), as further demonstrated in tomographic sections (Fig. 1 *F*, *ii*), where Xi heterogeneity contrasted with the clustered pattern seen in the Xa (Fig. 1 *E*, *ii*). The original A/B organization is therefore not evident in the Xi. To quantify mixing of A/B regions during the Xa to Xi transition, we computed a mixing ratio, $R_{A/B}$, by calculating the number of interactions between A and B compartment beads, divided by the total number of interactions made by beads in the B compartment, both with other A compartment beads and with B compartment beads. This ratio increased during XCI by ∼10% (*SI Appendix*, Fig. S3). On the other hand, when the ratio was computed for interactions between B regions ($R_{B/B}$), the ratio decreased due to B mixing with A. These data indicate that interactions between intra-B interactions were exchanged for interactions inter-A/B interactions during XCI.

The calculated mixing of A/B compartments is consistent with the idea that A and B compartments are merged to create S1 and S2 compartments, an intermediate and transitory state of the Xi prior to assuming its final superstructure (35). While S1/S2 compartments emerge only transiently on a Hi-C contact map during XCI, they become stable structures in cells deficient for the noncanonical SMC protein, SMCHD1 (35, 51–53). To examine the 3D relationship between A/B and S1/S2 structures, we produced 3D reconstructions of the Xi in SMCHD1 knockout cells and overlayed the previously mapped S1/S2 regions onto the 3D structure (Fig. 2 *A* and *B*). Our 3D reconstruction showed that the S1/S2 regions partitioned into two opposite faces on the Xi, with the S1 (Fig. 2*A*, green) compartment forming a roughly continuous surface on one side of the Xi and the S2 (Fig. 2*A*, purple) compartment forming a continuous surface on the opposite side. Cross-sections revealed that this organization extended beneath the surface (Fig. 2 *A*, *i*). The partition occurred nearly orthogonally to the CEN/TEL axis (Fig. 2 *A*, *ii*) and to the axis of the two megadomains (Fig. 2 *A*, *ii*). The megadomains persisted despite the SMCHD1 deficiency (Fig. 2*B*). Overall, the simulated contact map closely approximated the empirically measured heat map (Fig. 2*B*) ($R_{cp} = 0.97$, $R_{Pearson} = 0.85$).

To understand how A/B regions of the Xa transitions into S1/S2 regions of the Xi, we overlaid the A/B (red/blue) chromatin of the Xa onto the 3D structure of the SMCHD1 knockout Xi (Fig. 2 *A*, *iii*) and compared the red/blue (A/B) distribution with the green/purple (S1/S2) distribution. Surprisingly, the resulting overlay showed that portions of the original A/B structures remained intact beneath the S1/S2 organization. The A/B and S1/S2 organizations were not identical, as indeed the red/blue segments crossed over the axis of the S1/S2 structure. Thus, contrary to the prevailing belief that A/B organization is destroyed during XCI, it appears that elements of these original structures persist but remain hidden from view.

To examine the relationship between S1/S2 structures and the compartmentless Xi, we mapped S1/S2 regions of the SMCHD-deficient Xi onto the 3D model of the WT Xi (Fig. 2*C*). In contrast to the S1/S2 spatial partitioning observed for the mutant Xi (Fig. 2*A*), the S1/S2 (green/purple) segments as mapped onto the WT Xi showed less distinct compartmentalization in 3D physical space (Fig. 2*C*). Indeed, a cross-section of the 3D structure showed a greater degree of S1/S2 spatial mixing when comparing the SMCHD-deficient Xi with the WT Xi (compare Fig. 2 *A*, *i* with Fig 2 *C*, *i*). Even so, large 3D clusters of S2 (purple) and S1 (green) chromatin could still be observed. These observations suggest that S1/S2 3D organization may be less prominent, but not necessarily destroyed when the megadomain structures (Fig. 2*D*) form on the Xi. The megadomains identified by our simulation closely matched those empirically derived (Fig. 2*D*). Thus, neither the A/B nor S1/S2 3D organization appears to be entirely destroyed during the progressive Xa to Xi transformation. Notably, these hidden structures were not visible in a Hi-C contact map or by PCA underneath the obvious megadomains. Thus, our simulations enabled visualization of hidden 3D structures not discernible in a 2D connectivity map.

Spatiotemporal Evolution from Xa to Xi. To examine how transcriptional activity correlates with X chromosome shape, we tracked changes in volume and surface area as a function of time from day 0 (pre-XCI), day 3 (early XCI), to day 7 (mid-XCI) (Fig. 3 *A* and *B*). During this transition, the X chromosome underwent substantial volume compaction (Fig. 3*A*), supporting the general correlation between compaction and gene silencing (*SI Appendix*, Fig. S3). However, the surface area did not change dramatically with respect to volume during this timeframe. To examine differential spatial distributions of genes that are subject to XCI versus XCI escapees, we tracked their radial distributions (Fig. 3*C*) and asked if each is localized to the core, peripheral, or surface positions of the chromosome. Most silent genes localized within the core of the chromosome, while escapees tend to reside in the outer regions near the chromosome surface, either at or just beneath the surface, consistent with previously published cytological data (43, 54). To quantitatively assess the rearrangement in 3D architecture from Xa to Xi, we calculated the root mean squared distances (RMSD) between particles in Xi and Xa in a

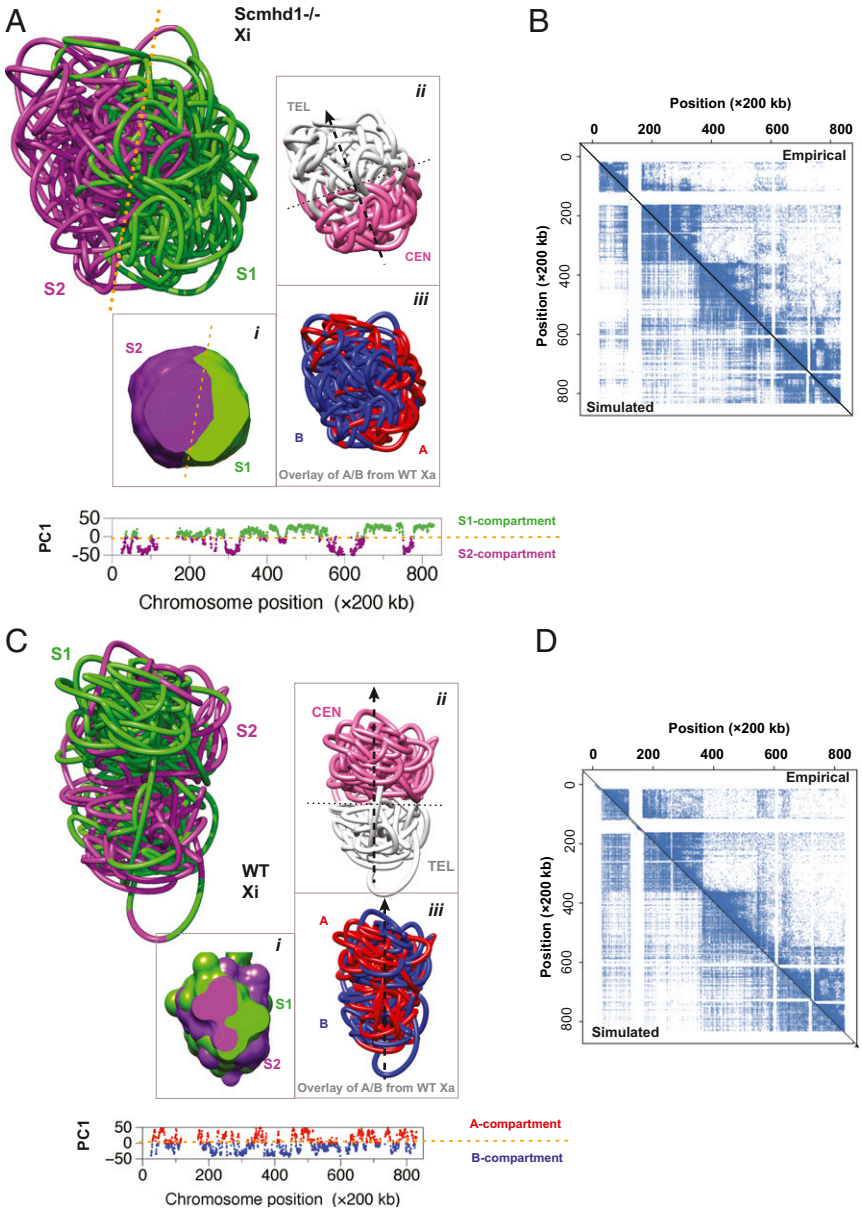

Fig. 2. Three-dimensional reconstruction of S1/S2 compartments of the Xi. (*A*) S1/S2 compartments of the Xi in SMCHD1-deficient cells. Green, positive PC1 values; purple, negative PC1 values. (*Inset i*): Cross-section; (*ii*) regions corresponding to megadomains; (*iii*) PC1 from Xa projected onto Xi (red, positive PC1 values; blue, negative PC1 values); (*Lower*) PC1 vs. 1D sequence position shows that A and B compartments are mixed in 1D sequence space. Orange dashed lines roughly delineate separation between S1 and S2 regions. Black thick dashed line, CEN/TEL axis. Black thin dashed line, perpendicular to CEN/TEL axis. (*B*) Experimental (*Upper* triangle) vs. simulated (*Lower* triangle) contact map for the Xi in SMCHD1 knockout cells. (*C*) Three-dimensional reconstruction of WT Xi: S1/S2 compartments mapped onto the WT Xi model showing mixing of S1/S2 compartments. Black thick dashed line, CEN/TEL axis. Black thin dashed line, perpendicular to CEN/TEL axis. (*D*) Experimental (*Upper* triangle) vs. simulated (*Lower* triangle) contact map for the WT Xi.

shell at each radius, r_{center}, and plotted them as a function of r_{center} (Fig. 3*D*). Interestingly, some escapees appeared to be clustered at or just beneath the Xi surface in our 3D model (Fig. 3*E*). A recent Hi-C analysis also suggested clustering of some escapee genes (55).

By combining the analysis of radial densities and chromosome segment displacements during XCI progression, we inferred that the Xi likely becomes more densely packed in its core. The core could have become too dense to allow further rearrangement of segments buried inside the core, resembling the principle of dynamical arrest in polymer glasses (Fig. 4), and differing dramatically from the unconstrained equilibrium globule collapse (Fig. 4 and *SI Appendix*, Fig. S2). In order to confirm the presence of dynamical arrest in chromosomes, we looked at the intermediate scattering function (the Fourier transform of the van Hove correlation function) of MD trajectories of chromosome motions (Fig. 4*E*), confirming that the intermediate scattering function did not decay to zero for chromosomes both in their active and inactive states, suggesting that chromosome dynamics is arrested. The difference in density between the core and surface (Fig. 3*E*) suggested that more architectural reorganization occurred on the surface where lower polymer density would allow for greater mobility (56). The lower density at the surface would facilitate diffusion, mixing, and entry of necessary transcription factors into the chromosome territory, possibly explaining why active genes and escapees reside near the surface.

We then asked whether, once formed, the Xa and Xi continue to evolve dynamically. We calculated relative contact probabilities as a function of spatial separation in Xa and Xi 3D models and asked which of the two modes they represent: a fully mixed unconstrained folded equilibrium polymer or a "glassy globule" that does not mix as a result of dynamical arrest (Fig. 4 *A*–*D*). A fully mixed folded polymer would be expected to have a single slope (Fig. 4*A*), whereas a chromosome with no mixing would be expected to have a curve with two slopes and contain far fewer long-range interactions relative to the fully mixed configuration (Fig. *4B*). Analysis of the Xa and Xi showed that both chromosomes have two slopes, indicating that relatively little mixing occurs in both the Xa and Xi states (Fig. 4 *C* and *D*). Altogether, these data suggest that there is dynamic reorganization during XCI as the X chromosome transits through A/B, S1/S2, and

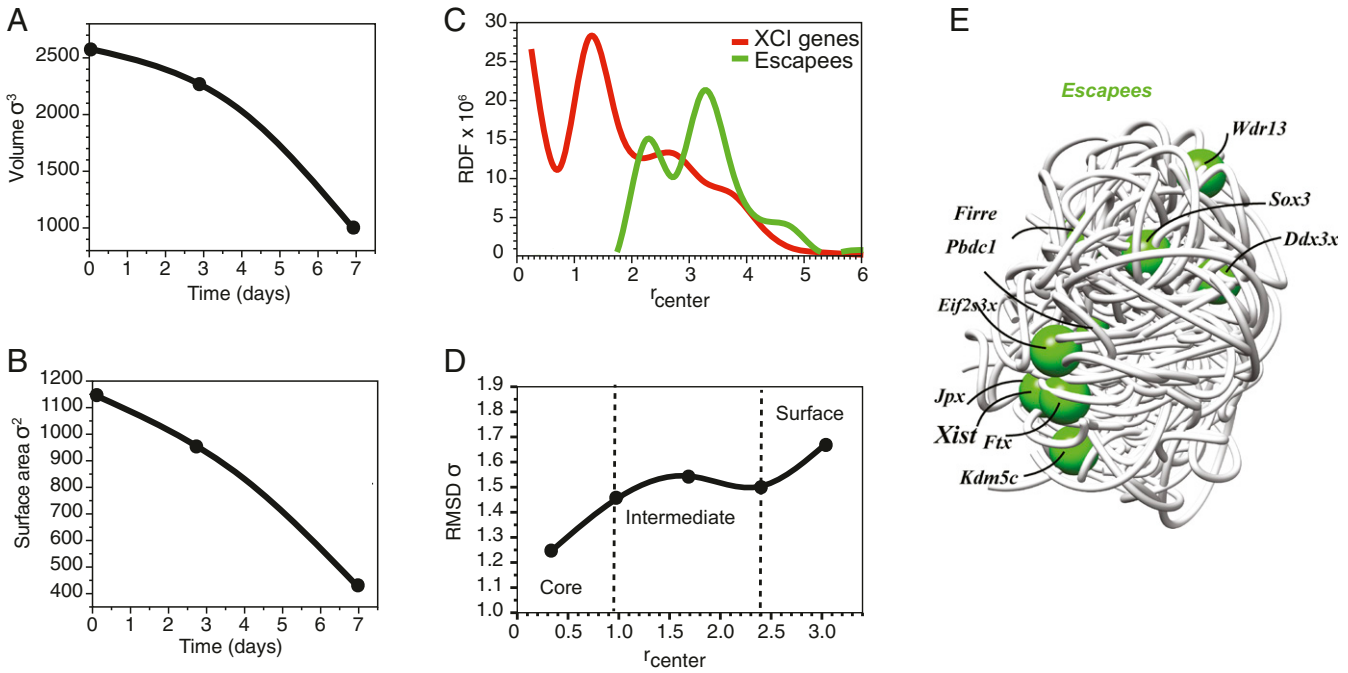

Fig. 3. Volume and surface area evolution over time. (*A*) Volume σ^3 (σ is a distance in reduced units) changes over time. (*B*) Surface area changes over time. (*C*) Radial distribution function of XCI and escape genes as a function of position from the center of the WT Xi chromosome taken from mouse embryonic fibroblasts. (*D*) RMSD as a function of position from the center of the chromosome during the transition from Xa to Xi. Chromosome is arbitrarily divided into core (innermost), intermediate, and surface. (*E*) Three-dimensional reconstruction of the WT Xi with escapee genes represented as green spheres. Escapees generally localize at or near surface.

megadomain structures (Fig. 3), but that, once formed, both Xa and Xi chromosomes are each in a state of dynamical arrest. To confirm this, we computed the intermediate scattering function (Fig. 4*E*), showing that indeed, for a mixed polymer, the function decays to zero, and in the case of Xa and Xi, it does not, consistent with the notion of dynamical arrest. We then used social network analysis as a method of investigating the change in global connectivity of the X chromosome during inactivation. We applied this analysis to our 3D Xa and Xi models, along with an unconstrained equilibrium polymer model as a control (Fig. 4 *F*–*H*). We represented the connectivity of the chromosome by a graph, where the degree of a node defines the number of contacts for that node and the local clustering coefficient measures the degree to which nodes cluster. Degree centrality measures the number of connections a particular node has in the network. The results displayed a visible difference in two types of models: unconstrained equilibrium polymers (Fig. 4*F*) and Hi-C constrained chromosome structures (Fig. 4 *G* and *H*). The nodes in fully mixed folded equilibrium polymers are more uniformly connected (interaction density smoothly decaying as a function of distance from the center of the graph) with no obvious clustering, as opposed to Hi-C–constrained chromosome models, where we identified a number of nodes with high connectivity that form a single cluster, which may play an important role in structure-based information spreading both locally and globally.

We also examined connectivity and mixing between the two megadomains of the Xi (Fig. 5). Although the long-range interactions seen within Xi megadomains are not present in the Xa Hi-C map, the regions corresponding to the proximal (Fig. 5*A*, white) and distal (Fig. 5*A*, purple) megadomains still exhibited compact globular morphologies that were spatially separated, and this separation persisted through the XCI time course. In the proximal megadomain at day 0, connectivity was relatively localized, with regions connected to each other that were nearby each other in linear sequence. For each megadomain, we colored the chromosome by linear sequence position, with red indicating regions nearer the CEN end of the megadomain, blue indicating regions nearer the TEL end, and white regions in between (Fig. 5*B*). Red, white, and blue segments were clearly separated at day 0. As XCI progressed, the Xi segments displayed more color mixing within the megadomain, indicating significantly more long-range interactions, consistent with the appearance of large "squares" of the megadomains on the empirically measured Hi-C map (Fig. 5*B*, days 3 and 7). The intramegadomain mixing could be seen from two other 3D perspectives of the structure (Fig. 5*C* and *SI Appendix*, Fig. S4). In the case of the proximal megadomain, similar intramegadomain mixing was observed, with clear separation between red, white, and blue at day 0 and progressively more mixing of red, white, and blue at days 3 and 7 (Fig. 5 *D* and *E* and *SI Appendix*, Fig. S4). Evident was a progression from mainly nearest-neighbor local interactions at day 0, typical of A/B compartments of the Xa, to increasingly longer-range interactions that represent S1/S2 compartments and, ultimately, the megadomains of the Xi.

To quantify the intramegadomain mixing of regions inside megadomains, we divided regions corresponding to megadomains evenly into three subregions (region 1, region 2, and region 3 in Fig. 5 *F*–*K*). The mixing ratio for each region, R_i, was determined by computing the number of interactions within a cutoff radius, R_c, between region i and another region divided by the total number of interactions. That is, for subregion 1, three values of R_1 were computed: one describing interactions of region 1 with itself, one describing interactions of region 1 with region 2, and one describing interactions of region 1 with region 3. In the case of megadomain 1 (Fig. 5 *F*–*H*), as expected, self-interactions (region 1 with region 1) decreased from day 0 to day 7. Interregional interactions within a megadomain (interactions of region 1 with region 2; interactions of region 1 with region 3) increased significantly from day 0 to day 7, demonstrating the occurrence of substantial mixing between these subregions within the megadomain during Xi. Similar behavior is observed for R_2 and R_3, suggesting that all three subregions were significantly mixed, consistent with the graphical representations of the 3D reconstructions in Fig. 5. Likewise, we also observed substantial mixing between

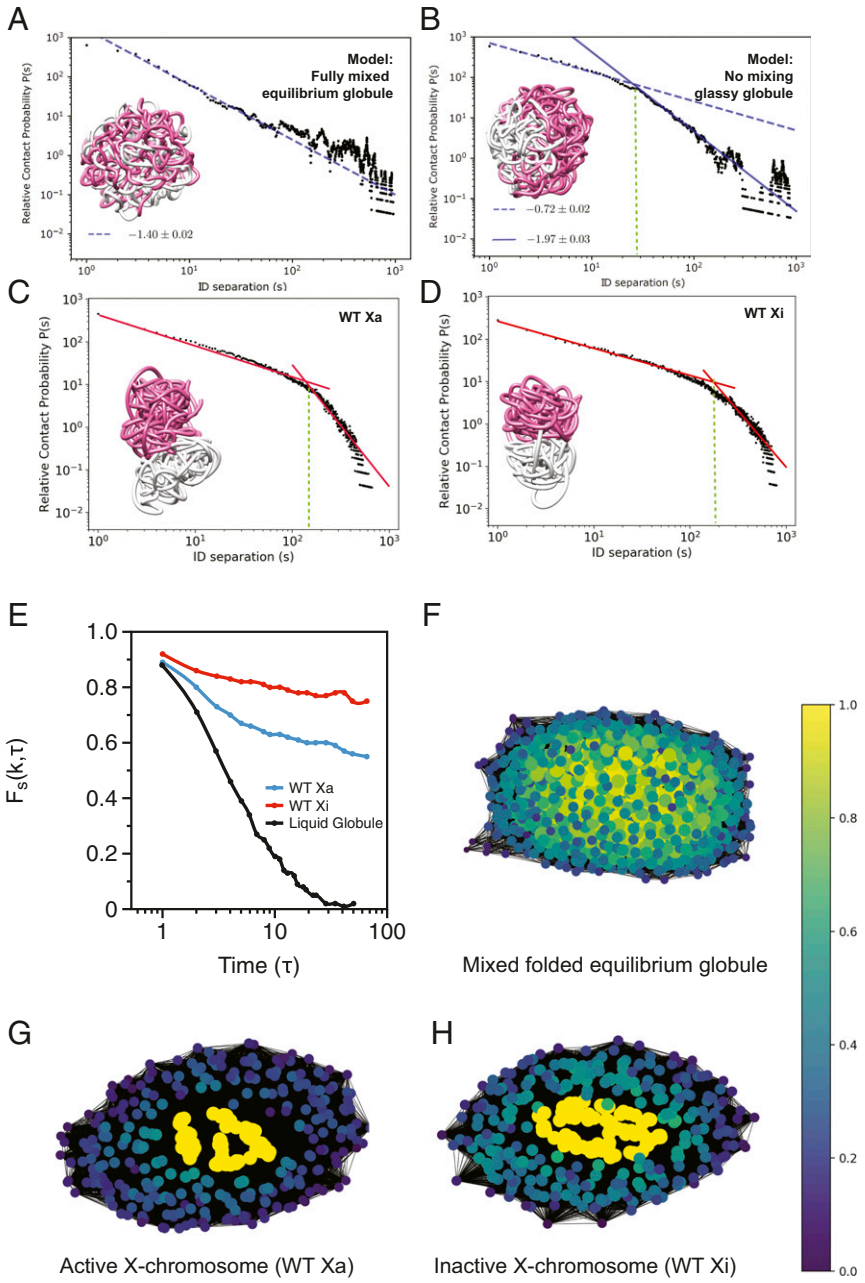

Fig. 4. Modeling the mixing of chromatin on the Xa and Xi. (*A*) Three-dimensional model and contact probabilities for a hypothetical fully mixed polymer chain. In the contact probability graph, a single slope suggests high degree of mixing. Pink, the region corresponding to megadomain 1 (positions 0 to 73 Mb); white, the region corresponding to megadomain 2 (positions 73 to 166 Mb). "ID separation" represents the node separation distance. (*B*) Model of a dynamically arrested glassy polymer chain with no mixing. Two slopes suggest two modes of connectivity: one at shorter ranges, one at longer ranges. (*C*) Model of the WT Xa showing contact probabilities defined by two slopes, suggesting that there is reduced mixing between the CEN (pink) and the TEL (white) domains and that there are two modes of connectivity: short and long range. (*D*) WT Xi model likewise shows contact probabilities with two slopes, indicating reduced mixing and two modes of connectivity: short and long range. (*E*) Self-intermediate scattering function $F_s(k, \tau)$ demonstrates arrested dynamics behavior typical for a glassy polymer. Both Xa and Xi show this behavior. For the liquid globule, the $F_s(k, \tau)$ decays to zero, typifying a fully mixed equilibrium globule (no Hi-C constraints). (*F–H*) Profiles showing normalized betweenness centrality for (*F*) folded equilibrium globule polymer chain, (*G*) WT Xa, and (*H*) WT Xi. Values near 0 (purple) indicate low number of interacting neighbors. Values near 1 (yellow) indicate high number of interacting neighbors. Small node size indicates low number of interactions. Large node size indicates high number of interactions.

subregions of megadomain 2 (Fig. 5 *I–K*). These results demonstrate that, although the regions corresponding to the two megadomains appear spatially distinct in Xa and Xi, subregions within these megadomains undergo significant mixing during the Xa to Xi transformation (Fig. 5) and then become stably "phase-separated" after XCI is established (Fig. 4).

A Model for Xist RNA Spreading in 4D. We endeavored to model how Xist RNA spreads in 4D by integrating Xist binding data and H3K27me3 enrichment data with our 3D chromosome models across time. Epigenomic methods, such as capture hybridization analysis of RNA targets (CHART), have produced genome-wide binding maps for Xist RNA across time and yielded the hypothesis that Xist RNA spreads through proximity transfer (57, 58), but Xist RNA's spreading trajectory in 3D has yet to be elucidated. We integrated data from time-course Hi-C and CHART experiments (35, 51, 58) from WT cells (Fig. 6*A*) by superimposing the 1D signal onto the deduced 3D structure of the chromosome. Our modeling indicated that the *Xist* gene localized at the surface of the Xa, specifically on the A-compartment side (Fig. 6*A*, day 0, *ii*). Intriguingly, our modeling indicated that, although *Xist* resides in the A compartment, it is located at the interface between the A and B hemispheres (Fig. 6*A*, day 4). Xist RNA was synthesized within the A compartment and, at day 4, spread along the ipsilateral side to cover the proximal A compartment hemisphere of the Xi (Fig. 6*A*, red-colored polymer segments coinciding with the A compartment in *ii*). The axis of the A/B compartments was perpendicular to the CEN/TEL axis (Fig. 6*A*, day 4, *iii*). A tomographic section through the Xi at day 4 revealed that Xist covered not just the surface of the A hemisphere, but also regions within its core. Thus, Xist RNA does not just travel along the surface of the Xi. By day 7, Xist had spread to the opposite hemisphere, now covering what were clearly separated A/B hemispheres of the former Xa. At the day 7 time point,

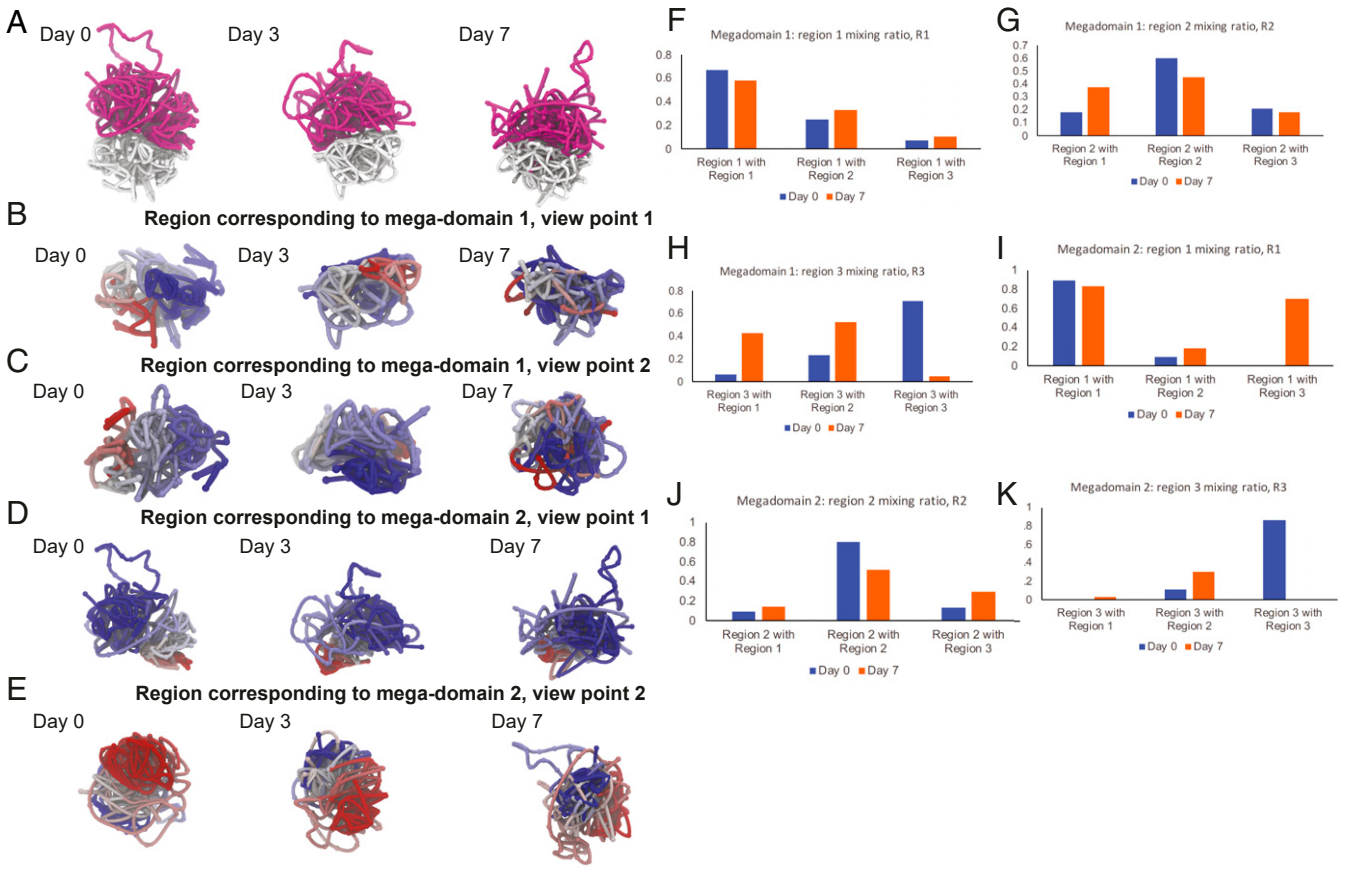

Fig. 5. Mixing of megadomains during XCI. (*A*) Three-dimensional reconstructions of the X chromosome based on Hi-C maps at days 0, 3, and 7. Pink, the region corresponding to megadomain 1 (positions 0 to 73 Mb); white, the region corresponding to megadomain 2 (positions 73 to 166 Mb). (*B*) Three-dimensional views of region corresponding to megadomain 1 (positions 0 to 73 Mb), from same 3D viewpoint as *A*. Chromosome is colored in a gradient from red to blue according to sequence position. At day 0, colors are separated. At day 7, colors are mixed, indicating intradomain mixing. (*C*) Same as *B*, but from a second viewpoint showing mixing at day 7. (*D*) Three-dimensional reconstructions based on Hi-C for region corresponding to megadomain 2 (positions 73 to 166 Mb), from same 3D viewpoint as *A*. Chromosome is colored in a gradient from red to blue according to sequence position. At day 0, colors a separated. At day 7, colors are mixed, indicating intradomain mixing. (*E*) Same as *D*, but from a second viewpoint showing mixing at day 7. (*F–K*) Quantification of intradomain mixing of regions corresponding to the two megadomains. (*F*) To quantify mixing within the region corresponding to megadomain 1, this region is divided evenly into three subregions (region 1, region 2, and region 3). The mixing ratio for region 1, R1, is determined by computing the number of interactions between region 1 and another region divided by the total number of interactions. Self-interactions (region 1 with region 1) decrease from day 0 to day 7. Intradomain interactions (e.g., region 1 with region 2) increase from day 0 to day 7. (*G*) The mixing ratio for region 2, R2, is determined by computing the number of interactions between region 2 and another region divided by the total number of interactions. (*H*) The mixing ratio for region 3, R3, is determined by computing the number of interactions between region 3 and another region divided by the total number of interactions. (*I–K*) Same as *F–H* but for region corresponding to megadomain 2.

however, it was also clear that the A/B compartments have ostensibly mixed and condensed (Fig. 6*A*, day 7, *ii*). Because Xist is known to spread with PRC2, we also examined the spreading dynamics of the Polycomb mark on trimethylated histone H3-lysine 27 (H3K27me3). The spreading of the H3K27me3 mark paralleled the migration of Xist RNA. Thus, Xist RNA, along with the epigenetic complexes that it recruits, emanates from a single point source in the A compartment and diffuses in 3D space both along the chromosomal surface as well as beneath.

Given the above, we next asked how the absence of SMCHD1 and failure to merge S1 and S2 compartments influenced the spreading dynamics of Xist RNA and H3K27me3. We mapped Xist CHART and H3K27me3 chromatin immunoprecipitation data onto the 3D reconstruction of the Xi in SMCHD1-deficient cells, and then projected the S1 (Fig. 6*B*, green) and S2 (Fig. 6*B*, purple) compartments onto the same model. Intriguingly, Xist RNA and H3K27me3 now only decorate one face of the Xi—specifically the S1 (Fig. 6*B*, green) compartment at day 7—at a time when Xist ordinarily would have already spread to the opposite face of the Xi (Fig. 6*A*). Thus, Xist stalled in the S1 compartment and failed to spread to the S2 half of the Xi. Likewise, H3K27me3 was observed to be enriched on the S1 side of the Xi, unable to continue onward to the S2 side. While these data are consistent with previous 1D and 2D findings that Xist RNA and PRC2 become trapped in the S1 domain when SMCHD1 is lost (51), we were able to visualize compartments in relation to the migration pattern of Xist RNA and PRC2 along the 3D surfaces of the A/B and S1/S2 type of chromatin across time, thereby characterizing the process in 4D.

Here we were also able to study Xist RNA's spreading through the radial distribution function. Whereas Xist spread outwardly in WT cells, Xist could not do so in SMCHD1-deficient cells beyond 4σ (Kolmogorov–Smirnov statistic = 0.49, $P = 1.33e^{-11}$) (Fig. 6*D*). In the SMCHD1-deficient Xi, escapees partitioned into the S1 hemisphere, whereas constitutive lamin-associated domains (cLADs) and constitutive interlamin domains (ciLADs) were distributed across the S1 and S2 hemispheres (Fig. 6 *E* and *F*).

Finally, we endeavored to visualize the formation of Xist RNA cloud around Xi during spreading and to investigate the spreading mechanism, we performed particle-based reaction diffusion simulations (59). This method is similar to the simulation method described above, but allows for additional processes, including chemical reactions, particle creation (e.g., transcription), and

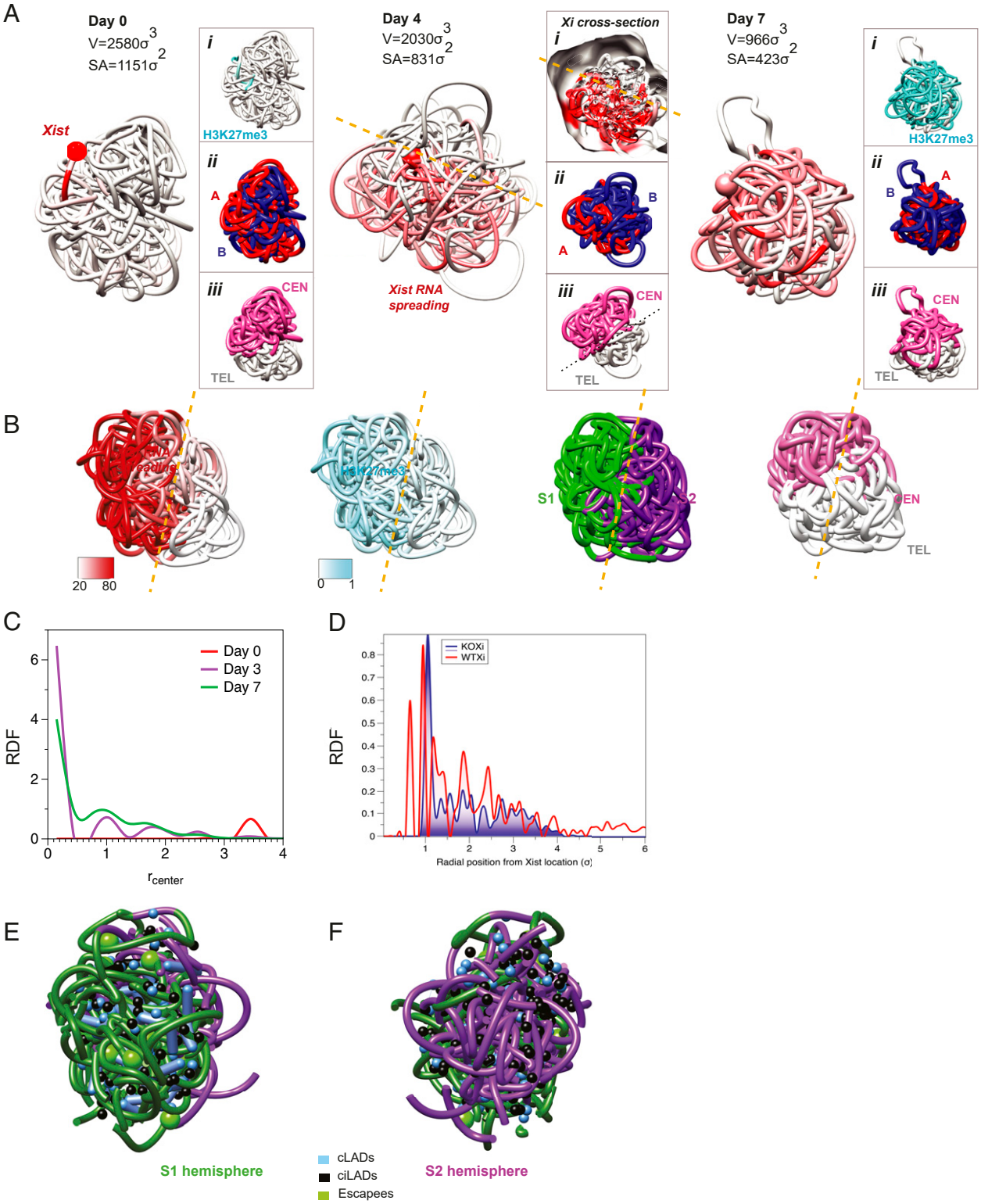

Fig. 6. Dynamics of Xist RNA spreading across hemispheres of the Xi. (*A*) Three-dimensional localization of Xist RNA (red) on the chromosome in pre-, early-, and mid-XCI (days 0, 3, 7). (*Insets*): (*i*) Localization of H3K27 methylation in the same orientation of the chromosome; (*ii*) localization of A and B compartments in the same orientation of the chromosome; (*iii*) localization of TEL and CEN domains in the same orientation of the chromosome. (*B*) Localization of Xist RNA, H3K27 methylation, S1/S2 compartments and CEN vs. TEL halves in the SMCHD1 knockout chromosome: both methylation and Xist occupy the S1 compartment that is orthogonal to the axis of CEN and TEL domains. (*C*) Radial distribution function as a function of radial position from Xist location for days 0, 3, and 7 (red, blue, and green curves, respectively). (*D*) Radial distribution function as a function of radial position from Xist location demonstrates the differences between Xist RNA spreading between the WTXi (red curve) and SMCHD1 knockout (blue curve) chromosomes. (*E*) Localization of cLADs, and ciLADs and escape genes on the S1 and (*F*) S2 hemispheres of the inactive chromosome in 3D as described in *E*.

binding. Specifically, we simulated similar 3D transitions to those described above (from Xa to Xi) subject to the same Hi-C constraints, with the additional effects of RNA transcription, RNA diffusion and RNA binding to the chromosome. Consistent with above findings, our reaction-diffusion model used the X-inactivation center (*Xic*) as the single point source from which Xist RNAs are transcribed (Fig. 7, purple sphere). As each bead in the chromosome represented 200 kb (consistent with the 200-kb Hi-C resolution), each Xist RNA (~15 kb) was modeled by a single particle. In our simulations, once transcribed, RNAs were allowed to freely diffuse in 3D space around and through the chromosome, subject to crowding by the cellular environment, emulated with spherical boundary conditions. RNAs could then bind back to the chromosome with a given rate, $k_{binding}$, to designated Xist binding sites, as determined experimentally by our CHART experiments (35, 51). In accordance with the above 3D reconstructions (Fig. 6), Xist RNA was simulated to initially diffuse from the proximal hemisphere, along the surface as well as through the internal core (Fig. 7 and Movie S2). Simultaneously, the X chromosome underwent large conformational changes during the transition from the Xa to Xi state (Fig. 7 and Movie S2). Rates and parameters were chosen consistent with experimental observations, with the transition from Xa to Xi occurring on the time scale of 7 d and RNA spreading occurring over 7 d. Our data suggest that crowding and diffusion were sufficient to achieve rapid spreading of Xist over the full X chromosome. Specifically, as the *Xic* moved from its Xa to Xi position in 3D, Xist RNAs quickly formed a cloud around the chromosome, maintained by crowding, and were positioned to cover the surface of the full chromosome (Fig. 7 and Movie S2). Simultaneously, the RNA particles initiating at the *Xic* diffused through the chromosome, coating the interior regions. A third effect occurred where RNA particles diffused into solution around the chromosome and then entered the chromosome from surface regions distal from the *Xic*, allowing more rapid coating of the intermediate layer between the surface and core (mantle).

Control simulations that allowed RNA diffusion but did not allow conformational change of the chromosome (i.e., "frozen" chromosome) showed less occupancy of Xist RNA binding sites on the chromosome, suggesting the specific conformational changes undergone by the X chromosome may help optimize the process of Xist coating through the various modes of Xist RNA binding. It is worth noting that the changes in 3D conformation of the X chromosome did not occur independently of spreading. We anticipate that 3D changes are highly connected with Xist and Polycomb spreading, with the latter also helping to propagate the former. As more experimental evidence elucidates this relationship, we hope to incorporate such interdependency in our models in the future. In sum, our time-evolution snapshots from particle-based reaction diffusion simulations suggest that diffusive processes alone may explain Xist RNA spreading, but does not rule out active processes in vivo.

Discussion

The 4DHiC pipeline is transferable and can be applied by a user to any Hi-C map and incorporated into existing empirical pipelines, such as GAM (60). By combining 2D Hi-C experiments with polymer physics models and reaction-diffusion kinetics, we have constructed 4D models to demonstrate the organization and the dynamical properties of the X chromosome during the transition from the active to the inactive state. From our 3D modeling, we have learned details that were not previously deduced from 2D datasets. First, previous studies left open the question of whether the original underlying structures are destroyed when an Xa is reorganized to an Xi. However, by visualizing specific 3D relationships and examining cross-sections of the Xa and Xi, our 4DHiC analysis suggests that neither the A/B compartments nor the S1/S2 structures are wholly destroyed within the Xi superstructure. Second, because of limitations associated with viewing 2D information alone, the Xi previously gave the appearance of being unstructured within two megadomains. Taken together with published studies, our 4DHiC analysis now underscores the fact that the Xi incorporates structural remnants from an earlier configuration in the chromosome's life cycle. Third, our study identifies three layers of chromosome dynamics: slow dynamics in the dense core, intermediate layer (mantle), and fast dynamics on the surface of the chromosome where gene expression continues to take place (escapees). During the XCI time course, the X chromosome transits through A/B, S1/S2, and megadomain structures by undergoing a highly dynamic but regulated mixing to assume new structures. However, once formed, the folded Xa and Xi are analogous to a glassy polymer where little additional global mixing of genetic elements occurs. In essence, once formed, domains of the Xa and Xi are stably phase-separated.

From our 4D study we have also learned that the *Xist* gene—although located in the A compartment—resides near the A/B interface. During XCI, Xist RNA originates in the A compartment, and spreads through both the surface and the core of the A compartment initially. Xist RNA then depends on SMCHD1 to migrate across the A/B interface to spread over the B compartment. Within both hemispheres, Xist binds both surface and core chromatin. Our 3D analysis provides an effective way of tracking the spreading of Xist RNA, showing that the spreading resembles a diffusive wave-front emanating from a single point source, the *Xist* locus. In the SMCHD1 knockout case, the wave-like propagation halts midway, effectively polarizing the chromosome, only half of which becomes covered by Xist RNA. Xist's coverage of chromosome surface versus its core could not be determined from 2D contact maps alone. It is also notable that escapees reside near or at the surface of the Xi where the chromosome is less compact and where greater mobility is possible. Our deductions (Figs. 6 and 7) are consistent with the wealth of published 2D contact maps (7, 35–38, 51, 61, 62) and microscopy data that have yielded much valuable information about locations of select genes within the Xi territory (40–46). The picture emerges of a well-organized but dynamic Xi during its formation and establishment, and then a spatially phase-separated glassy globule once the Xi is established. Taken together, our results are consistent with a gradual accumulation of structural elements throughout the process of Xi, whose 4D architecture may aid in accelerating Xist diffusion and binding throughout the chromosome, ultimately resulting in rapid Xist coating and shutdown of the X chromosome.

Methods

Simulations described in this work were performed using the large-scale atomic/molecular massively parallel simulator (63) and reaction diffusion dynamics (ReaDDy2) (59). The initial structures consisted of $N = 833$ beads corresponding to ~167 Mb. The initial configuration forms an open coil as a result of a self-avoiding random walk. Experimental Hi-C constraints were used directly such that connected segments were required to form harmonic bonds between interacting particles, and those were directed to form connected pairs prior to production simulations. The ReaDDy2 particle-based reaction diffusion simulation package was used to simulate RNA spreading around and through the X chromosome (59). Raw next-generation sequencing data and processed files for Hi-C, chromatin immunoprecipitation sequencing (ChIP-seq) and CHART-seq have been deposited in the Gene Expression Omnibus (https://www.ncbi.nlm.nih.gov/geo/) under accession no. GSE99991.

Data Availability. Previously published data were used for this work. All data and code used in the structure analysis are available in *SI Appendix* and Dataset S1. Raw next-generation sequencing data and processed files for Hi-C, ChIP-seq, and CHART-seq have been deposited in the Gene Expression Omnibus (accession no. GSE99991).

ACKNOWLEDGMENTS. We thank members of the K.Y.S. and J.T.L. laboratories for stimulating discussions. This work was funded by Los Alamos National Laboratory (LANL) Laboratory Directed Research and Development grant 20210082DR and LANL Laboratory Directed Research and Development grant 20210134ER (to K.Y.S. and A.L.), grant F31HD100109-01 (to A.K.), and NIH grant R01-HD097665 (to J.T.L.). We are grateful to LANL Institutional Computing for their generous support.

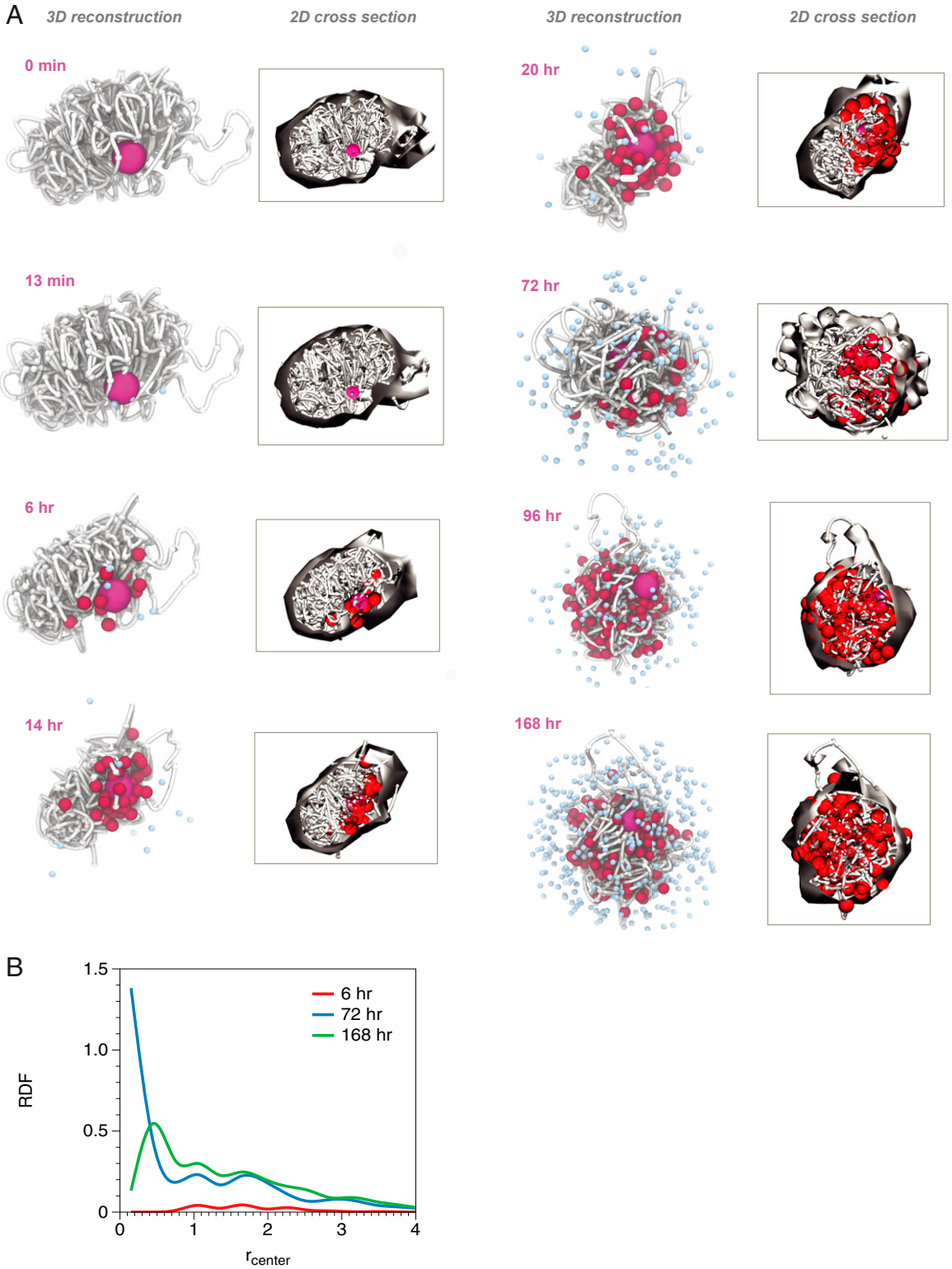

Fig. 7. Time-evolution snapshots from particle-based reaction diffusion simulations suggest that diffusive processes alone may explain Xist RNA spreading. (*A*) Time evolution of chromosome structures and Xist RNA particles, with corresponding cross-sections through the chromosome, displaying the interior of the chromosome (*Insets*). White chain, X chromosome; magenta, Xic; red, bound Xist RNA; light blue, diffusing Xist RNA. At time = 0 d, 13 min, newly transcribed Xist RNA particles visible (blue). At time = 0 d, 6 h, Xist RNAs begin binding to experimentally determined Xist binding sites (red). At time = 0 d, 14 h, RNA particles begin to penetrate interior of chromosome. At time = 0 d, 20 h, RNA particles reach core of chromosome (*Inset*). At time = 3 d, chromosome has undertaken large reorganization. At time = 4 d, 5 h, RNA particles cover much of X chromosome. At time = 7 d, Xist RNA has covered majority of measured Xist binding sites, including those in the interior. (*B*) Radial distribution function (RDF) for bound Xist RNA particles for 6 h, 72 h, and 168 h shows Xist RNAs gradually penetrate core of chromosome. The *x* axis is in units of σ.

1. G. D. Bascom, K. Y. Sanbonmatsu, T. Schlick, Mesoscale modeling reveals hierarchical looping of chromatin fibers near gene regulatory elements. *J. Phys. Chem. B* **120**, 8642–8653 (2016).
2. J. Jung *et al*., Scaling molecular dynamics beyond 100,000 processor cores for large-scale biophysical simulations. *J. Comput. Chem.* **40**, 1919–1930 (2019).
3. E. Lieberman-Aiden *et al*., Comprehensive mapping of long-range interactions reveals folding principles of the human genome. *Science* **326**, 289–293 (2009).
4. J. R. Paulson, U. K. Laemmli, The structure of histone-depleted metaphase chromosomes. *Cell* **12**, 817–828 (1977).
5. T. Cremer, C. Cremer, Chromosome territories, nuclear architecture and gene regulation in mammalian cells. *Nat. Rev. Genet.* **2**, 292–301 (2001).
6. J. R. Dixon *et al*., Topological domains in mammalian genomes identified by analysis of chromatin interactions. *Nature* **485**, 376–380 (2012).
7. S. S. Rao *et al*., A 3D map of the human genome at kilobase resolution reveals principles of chromatin looping. *Cell* **159**, 1665–1680 (2014).
8. E. de Wit *et al*., CTCF binding polarity determines chromatin looping. *Mol. Cell* **60**, 676–684 (2015).
9. J. Fraser, I. Williamson, W. A. Bickmore, J. Dostie, An overview of genome organization and how we got there: From FISH to Hi-C. *Microbiol. Mol. Biol. Rev.* **79**, 347–372 (2015).
10. A. C. Bell, G. Felsenfeld, Methylation of a CTCF-dependent boundary controls imprinted expression of the Igf2 gene. *Nature* **405**, 482–485 (2000).
11. D. G. Lupiáñez *et al*., Disruptions of topological chromatin domains cause pathogenic rewiring of gene-enhancer interactions. *Cell* **161**, 1012–1025 (2015).
12. M. Merkenschlager, E. P. Nora, CTCF and cohesin in genome folding and transcriptional gene regulation. *Annu. Rev. Genomics Hum. Genet.* **17**, 17–43 (2016).
13. Y. Guo *et al*., CRISPR inversion of CTCF sites alters genome topology and enhancer/promoter function. *Cell* **162**, 900–910 (2015).
14. E. M. Darrow *et al*., Deletion of DXZ4 on the human inactive X chromosome alters higher-order genome architecture. *Proc. Natl. Acad. Sci. U.S.A.* **113**, E4504–E4512 (2016).
15. J. H. I. Haarhuis *et al*., The cohesin release factor WAPL restricts chromatin loop extension. *Cell* **169**, 693–707.e14 (2017).
16. E. P. Nora *et al*., Targeted degradation of CTCF decouples local insulation of chromosome domains from genomic compartmentalization. *Cell* **169**, 930–944.e22 (2017).
17. S. S. P. Rao *et al*., Cohesin loss eliminates all loop domains. *Cell* **171**, 305–320.e24 (2017).
18. J. E. Froberg, S. F. Pinter, A. J. Kriz, T. Jégu, J. T. Lee, Megadomains and superloops form dynamically but are dispensable for X-chromosome inactivation and gene escape. *Nat. Commun.* **9**, 5004 (2018).
19. I. Williamson *et al*., Developmentally regulated *Shh* expression is robust to TAD perturbations. *Development* **146**, dev179523 (2019).
20. E. T. Fok, S. Fanucchi, K. Bystricky, M. M. Mhlanga, Visualization of chromatin dynamics by live cell microscopy using CRISPR/Cas9 gene editing and ANCHOR labeling. *Methods Mol. Biol.* **2157**, 197–212 (2021).
21. A. Goloborodko, M. V. Imakaev, J. F. Marko, L. Mirny, Compaction and segregation of sister chromatids via active loop extrusion. *eLife* **5**, e14864 (2016).
22. J. Paulsen *et al*., Chrom3D: Three-dimensional genome modeling from Hi-C and nuclear lamin-genome contacts. *Genome Biol.* **18**, 21 (2017).
23. K. Huang *et al*., Physical and data structure of 3D genome. *Sci. Adv.* **6**, eaay4055 (2020).
24. D. Jost, P. Carrivain, G. Cavalli, C. Vaillant, Modeling epigenome folding: Formation and dynamics of topologically associated chromatin domains. *Nucleic Acids Res.* **42**, 9553–9561 (2014).
25. M. Di Pierro, B. Zhang, E. L. Aiden, P. G. Wolynes, J. N. Onuchic, Transferable model for chromosome architecture. *Proc. Natl. Acad. Sci. U.S.A.* **113**, 12168–12173 (2016).
26. C. A. Brackey, D. Marenduzzo, N. Gilbert, Mechanistic modeling of chromatin folding to understand function. *Nat. Methods* **17**, 767–775 (2020).
27. A. Rosa, R. Everaers, Structure and dynamics of interphase chromosomes. *PLOS Comput. Biol.* **4**, e1000153 (2008).
28. F. Serra *et al*., Automatic analysis and 3D-modelling of Hi-C data using TADbit reveals structural features of the fly chromatin colors. *PLoS Comput. Biol.* **13**, e1005665 (2017).
29. Z. Duan *et al*., A three-dimensional model of the yeast genome. *Nature* **465**, 363–367 (2010).
30. J. Dekker, L. Mirny, The 3D genome as moderator of chromosomal communication. *Cell* **164**, 1110–1121 (2016).
31. M. F. Lyon, Gene action in the X-chromosome of the mouse (*Mus musculus* L.). *Nature* **190**, 372–373 (1961).
32. J. Starmer, T. Magnuson, A new model for random X chromosome inactivation. *Development* **136**, 1–10 (2009).
33. C. M. Disteche, Dosage compensation of the sex chromosomes. *Annu. Rev. Genet.* **46**, 537–560 (2012).
34. T. Jégu, E. Aeby, J. T. Lee, The X chromosome in space. *Nat. Rev. Genet.* **18**, 377–389 (2017).
35. C. Y. Wang, T. Jégu, H. P. Chu, H. J. Oh, J. T. Lee, SMCHD1 merges chromosome compartments and assists formation of super-structures on the inactive X. *Cell* **174**, 406–421.e25 (2018).
36. X. Deng *et al*., Bipartite structure of the inactive mouse X chromosome. *Genome Biol.* **16**, 152 (2015).
37. A. Minajigi *et al*., Chromosomes. A comprehensive Xist interactome reveals cohesin repulsion and an RNA-directed chromosome conformation. *Science* **349**, aab2276 (2015).
38. L. Giorgetti *et al*., Structural organization of the inactive X chromosome in the mouse. *Nature* **535**, 575–579 (2016).
39. G. Bonora *et al*., Orientation-dependent Dxz4 contacts shape the 3D structure of the inactive X chromosome. *Nat. Commun.* **9**, 1445 (2018).
40. C. M. Clemson, J. A. McNeil, H. F. Willard, J. B. Lawrence, XIST RNA paints the inactive X chromosome at interphase: Evidence for a novel RNA involved in nuclear/chromosome structure. *J. Cell Biol.* **132**, 259–275 (1996).
41. B. P. Chadwick, H. F. Willard, Multiple spatially distinct types of facultative heterochromatin on the human inactive X chromosome. *Proc. Natl. Acad. Sci. U.S.A.* **101**, 17450–17455 (2004).
42. J. Chaumeil, P. Le Baccon, A. Wutz, E. Heard, A novel role for Xist RNA in the formation of a repressive nuclear compartment into which genes are recruited when silenced. *Genes Dev.* **20**, 2223–2237 (2006).
43. C. M. Clemson, L. L. Hall, M. Byron, J. McNeil, J. B. Lawrence, The X chromosome is organized into a gene-rich outer rim and an internal core containing silenced nongenic sequences. *Proc. Natl. Acad. Sci. U.S.A.* **103**, 7688–7693 (2006).
44. K. Teller *et al*., A top-down analysis of Xa- and Xi-territories reveals differences of higher order structure at $\geq$ 20 Mb genomic length scales. *Nucleus* **2**, 465–477 (2011).
45. D. Smeets *et al*., Three-dimensional super-resolution microscopy of the inactive X chromosome territory reveals a collapse of its active nuclear compartment harboring distinct Xist RNA foci. *Epigenetics Chromatin* **7**, 8 (2014).
46. S. Wang *et al*., Spatial organization of chromatin domains and compartments in single chromosomes. *Science* **353**, 598–602 (2016).
47. A. Abbas *et al*., Integrating Hi-C and FISH data for modeling of the 3D organization of chromosomes. *Nat. Commun.* **10**, 2049 (2019).
48. G. S. Grest, K. Kremer, Molecular dynamics simulation for polymers in the presence of a heat bath. *Phys. Rev. A Gen. Phys.* **33**, 3628–3631 (1986).
49. A. Lappala, E. Terentjev, "Raindrop" coalescence of polymer chains during coil-globule transition. *Macromolecules* **46**, 1239–1247 (2013).
50. A. H. Horakova *et al*., The mouse DXZ4 homolog retains Ctcf binding and proximity to Pls3 despite substantial organizational differences compared to the primate macrosatellite. *Genome Biol.* **13**, R70 (2012).
51. C. Y. Wang, D. Colognori, H. Sunwoo, D. Wang, J. T. Lee, PRC1 collaborates with SMCHD1 to fold the X-chromosome and spread Xist RNA between chromosome compartments. *Nat. Commun.* **10**, 2950 (2019).
52. N. Jansz *et al*., Smchd1 regulates long-range chromatin interactions on the inactive X chromosome and at Hox clusters. *Nat. Struct. Mol. Biol.* **25**, 766–777 (2018).
53. M. R. Gdula *et al*., The non-canonical SMC protein SmcHD1 antagonises TAD formation and compartmentalisation on the inactive X chromosome. *Nat. Commun.* **10**, 30 (2019).
54. J. C. Chow *et al*., LINE-1 activity in facultative heterochromatin formation during X chromosome inactivation. *Cell* **141**, 956–969 (2010).
55. A. J. Kriz, D. Colognori, H. Sunwoo, B. Nabet, J. T. Lee, Balancing cohesin eviction and retention prevents aberrant chromosomal interactions, Polycomb-mediated repression, and X-inactivation. *Mol. Cell* **81**, 1970–1987.e1979 (2021).
56. A. Lappala, L. Sefton, P. W. Fenimore, E. M. Terentjev, Connectivity and free-surface effects in polymer glasses. *Sci. Rep.* **9**, 3830 (2019).
57. J. M. Engreitz *et al*., The Xist lncRNA exploits three-dimensional genome architecture to spread across the X chromosome. *Science* **341**, 1237973 (2013).
58. M. D. Simon *et al*., High-resolution Xist binding maps reveal two-step spreading during X-chromosome inactivation. *Nature* **504**, 465–469 (2013).
59. M. Hoffmann, C. Fröhner, F. Noé, ReaDDy 2: Fast and flexible software framework for interacting-particle reaction dynamics. *PLOS Comput. Biol.* **15**, e1006830 (2019).
60. L. Fiorillo *et al*., Comparison of the Hi-C, GAM and SPRITE methods using polymer models of chromatin. *Nat. Methods* **18**, 482–490 (2021).
61. E. Splinter *et al*., The inactive X chromosome adopts a unique three-dimensional conformation that is dependent on Xist RNA. *Genes Dev.* **25**, 1371–1383 (2011).
62. H. Marks *et al*., Dynamics of gene silencing during X inactivation using allele-specific RNA-seq. *Genome Biol.* **16**, 149 (2015).
63. S. Plimpton, Fast parallel algorithms for short-range molecular-dynamics. *J. Comput. Phys.* **117**, 1–19 (1995).